



Seeing protein monolayers with naked eye through plasmonic Fano resonances

Ahmet A. Yanik^{a,b,1}, Arif E. Cetin^{a,b}, Min Huang^{a,b}, Alp Artar^{a,b}, S. Hossein Mousavi^c, Alexander Khanikaev^c, John H. Connor^d, Gennady Shvets^c, and Hatice Altug^{a,b,1}

^aDepartment of Electrical and Computer Engineering, ^bThe Photonics Center, Boston University, Boston, MA 02215; ^cDepartment of Microbiology, Boston University School of Medicine, Boston, MA 02218; and ^dDepartment of Physics, University of Texas at Austin, Austin, TX 78712

Edited* by Erich P. Ippen, Massachusetts Institute of Technology, Cambridge, MA, and approved June 2, 2011 (received for review February 4, 2011)

We introduce an ultrasensitive label-free detection technique based on asymmetric Fano resonances in plasmonic nanoholes with far reaching implications for point-of-care diagnostics. By exploiting extraordinary light transmission phenomena through high-quality factor ($Q_{\text{solution}} \sim 200$) subradiant dark modes, we experimentally demonstrate record high figures of merits (FOMs as high as 162) for intrinsic detection limits surpassing that of the gold standard prism coupled surface-plasmon sensors (Kretschmann configuration). Our experimental record high sensitivities are attributed to the nearly complete suppression of the radiative losses that are made possible by the high structural quality of the fabricated devices as well as the subradiant nature of the resonances. Steep dispersion of the plasmonic Fano resonance profiles in high-quality plasmonic sensors exhibit dramatic light intensity changes to the slightest perturbations within their local environment. As a spectacular demonstration of the extraordinary sensitivity and the quality of the fabricated biosensors, we show direct detection of a single monolayer of biomolecules with naked eye using these Fano resonances and the associated Wood's anomalies. To fabricate high optical-quality sensors, we introduce a high-throughput lift-off free evaporation fabrication technique with extremely uniform and precisely controlled nanofeatures over large areas, leading to resonance line-widths comparable to that of the ideally uniform structures as confirmed by our time-domain simulations. The demonstrated label-free sensing platform offers unique opportunities for point-of-care diagnostics in resource poor settings by eliminating the need for fluorescent labeling and optical detection instrumentation (camera, spectrometer, etc.) as well as mechanical and light isolation.

surface plasmonics | subradiant dark resonances | biosensing | label free | global health

Surface plasmonics, the science and engineering of electromagnetic waves trapped at the metal/dielectric interfaces, has opened up a new realm of possibilities for a broad range of applications ranging from biosensing to photovoltaics (1–5). Within the last decade, functional components of unparalleled optical devices creating, manipulating and concentrating light at metal surfaces below the diffraction limit are shown (2, 6). Engineering of these functionalities have led to the demonstration of revolutionary concepts such as superlensing (7) and optical cloaking (8), as well as groundbreaking observations in nonlinear photonics (9) and all-optical manipulation (10). By concentrating electromagnetic fields thousands of times smaller than the diffraction limited volume of light, extremely strong light-matter interactions leading to orders of magnitude enhanced second harmonic generation (9), fluorescence (11), surface enhanced Raman scattering (12), and surface enhanced infrared absorption spectroscopy (13–16) are shown. Developments within the last decade seem to hint at a bright future for plasmonic devices.

In general, it is desirable to have high-quality factor plasmonic resonances and enhanced near-fields for stronger light-matter interactions. In practice though, both the radiative and nonradiative (ohmic) losses exist in nanoplasmonic devices and can

severely shorten the life-times of the plasmonic excitations. Advantages of plasmonic effects deteriorate with increasing losses in many applications. For example, in biosensing applications based on effective refractive index modulation, the detection limits strongly depend on both the refractive index sensitivity of the plasmonic resonances as well as the resonance line-widths (17). Narrower line-widths allow smaller resonance shifts (analyte concentrations) to be detected. In applications critically depended on light intensities, losses may limit the near-field enhancements. Hence, the realization of practical plasmonic devices strongly depends on our ability to control these decay channels. Nonradiative Drude (ohmic) damping processes are intrinsic to the metals. Radiative losses, on the other hand, can be effectively controlled (14, 18).

Surface roughness can cause stronger plasmon coupling to the continuum (scattering losses) leading to shorter plasmon propagation lengths and spectrally broader resonances. High-quality fabrication methods can help minimizing contributions of these radiative decay channels (19). Further enhancements of plasmonic lifetimes leading to narrower resonance line-widths can be achieved by engineering of light coupling mechanisms using collective excitations and tailored designs (14, 18). Subradiant dark modes are particularly promising for creation of high-quality factor plasmonic resonances due to their zero net-dipole moment character forbidding direct light coupling to the continuum. Another fundamental physical phenomenon, Fano resonance, with its asymmetric line shape and strongly dispersive character enables strong line-width narrowings (20). Plasmonic Fano resonances have been extensively studied in nanoparticle and metamaterial systems by coupling broad line-width superradiant and narrow line-width subradiant modes (4, 21–23). However, there are very limited studies on Fano resonances created through direct coupling of the dipolar incident light to subradiant dark modes (24).

In this letter, we experimentally demonstrate that strongly dispersive Fano phenomenon combined with subradiant dark modes can be exploited for ultrasensitive label-free biosensing. Our approach is based on direct coupling of incident-light to multipolar subradiant modes through retardation effects in plasmonic nanohole devices. By creating a distinct light coupling scheme allowing high numerical aperture (NA) imaging, we demonstrate extraordinary light transmission (EOT) resonances with remarkably narrow line-widths (approximately 4.29 nm) that are solely limited by the nonradiative Drude damping processes. By utiliz-

Author contributions: A.A.Y. and H.A. designed research; A.A.Y., M.H., and H.A. performed research; A.A.Y., A.E.C., M.H., A.A., S.H.M., A.K., J.H.C., G.S., and H.A. contributed new reagents/analytic tools; A.A.Y., A.E.C., G.S., and H.A. analyzed data; and A.A.Y. and H.A. wrote the paper.

The authors declare no conflict of interest.

*This Direct Submission article had a prearranged editor.

Freely available online through the PNAS open access option.

To whom correspondence may be addressed. E-mail: altug@bu.edu and yanik@bu.edu.

This article contains supporting information online at www.pnas.org/lookup/suppl/doi:10.1073/pnas.1101910108/-DCSupplemental.

ing such spectrally sharp extraordinary light transmissions, we show label-free biosensing with record high experimental figures of merit (FOMs as high as 162) for detection limits surpassing that of the gold standard prism coupled surface-plasmon sensors (25, 26). Extremely sharp plasmonic Fano resonances in high-quality plasmonic sensors also present dramatic intensity changes to slightest perturbations within their local environment. This intensity difference can be easily distinguished without using any optical detection instrument (camera and spectrometer, for example). By exploiting these Fano resonances and the associated high contrast ratios of the on-resonance to the off-resonance transmissions (Wood's anomaly), we demonstrate direct detection of a single monolayer of antibodies with naked eye. Such sharp resonances could open door to a new generation of ultra-portable and ultrasensitive plasmonic biosensors for detection of biologically important molecules and pathogens (27, 28). A crucial prerequisite for the record high sensitivities is the suppression of the scattering losses caused by surface roughness and in-homogeneities. To achieve this, we introduce an exceptional lift-off free evaporation (LIFE) lithography technique for high-throughput fabrication of plasmonic devices with extremely uniform and precisely controlled nano-features over large areas.

Results and Discussion

LIFE Nanolithography. Technique is summarized in Fig. 1 for the alternative schemes based on electron-beam lithography (EBL) and interferometric (IL) lithography, respectively. This technique eliminates the need for any ion milling and lift-off processes and allows fabrication of high optical-quality plasmonic devices (29). The EBL-based scheme (Fig. 1A) consists of three consecutive steps: (i) fabrication of the free standing membrane, (ii) patterning on the membrane with EBL and reactive ion etching, and (iii) direct deposition of metallic plasmonic devices (SI Text). Unlike, previous studies based on EBL, our fabrication method does not involve any lift-off processes, and uses well-established positive electron-beam resists. Interferometric lithography can be conveniently adapted for massively parallel fabrication of plasmonic devices over large areas. The IL-based scheme (Fig. 1B) consists of four consecutive steps: (i) spin coating of antireflection and photoresist layers, and wafer-scale patterning of plasmonic devices, (ii) side deposition of a metallic mask layer, and reactive ion etching of the SiN_x layer, (iii) fabrication of the free standing nanostructures using wet and reactive ion processes, and (iv) direct deposition of the metal layer (SI Text).

Experimentally measured resonance line-widths are a sound measure of the life-times of the plasmonic excitations that is controlled by the strength of the radiative and nonradiative (ohmic) decay channels. For a perfectly uniform device with

no structural in-homogeneity or surface roughness, the radiative decay processes are expected to be minimized (19). Fig. 2A shows the calculated (dashed line) and experimentally measured (solid line) transmission spectra of an e-beam fabricated device (with a periodicity of 600 nm and a nanohole aperture with $d = 200$ nm). Here, the Drude model parameters are obtained from previous experimental studies (30). Spectrally narrow plasmonic resonances (as narrow as $\Delta\lambda = 4.3$ nm) with Q -factors (as high as $Q_{\text{air}} = 195$) are demonstrated in our measurements. Close agreement of the experimental measured spectra with that of the finite difference time domain (FDTD) simulations demonstrates that our fabrication scheme enables fabrication of highly uniform structures with minimal surface roughness leading to resonance line-widths comparable to ideally uniform structures.

Subradiant Dark Modes in Extraordinary Light Transmission Phenomena

In our experimental measurements (Fig. 2A), multiple extraordinary light transmission resonances are observed with the creation of surface-plasmon polaritons (SPP) corresponding to the different grating orders. For a square lattice, the momentum matching condition between the in-plane wave-vectors of the incident photons and the surface-plasmon polaritons is fulfilled when the Bragg coupling condition $\vec{k}_{\text{sp}} = \vec{k}_x \pm i\vec{G}_x \pm j\vec{G}_y$ is met (31). Here \vec{k}_{sp} is the surface-plasmon wavevector, \vec{k}_x incident-light wave vector in- x direction (parallel to the metal surface), θ is the angle of incidence to the surface normal, (i, j) is the grating order for reciprocal lattice vector \vec{G}_x and \vec{G}_y of the square lattice ($|\vec{G}_x| = |\vec{G}_y| = 2\pi/p$, p is the periodicity). The wave-vector relation for the SPPs, within a first approximation, can be given as $|\vec{k}_{\text{sp}}| = (\omega/c) \sqrt{\epsilon_d \epsilon_m / \epsilon_d + \epsilon_m}$, where ω is the frequency of the incident light and ϵ_m/ϵ_d is the dielectric constant of the metal/interface-medium. Fig. 2B shows the spectral dispersion of transmission minima as a function of the angle of incidence for different grating orders. This diagram also provides a qualitative guide for the dispersive behavior of the resonant transmission maxima (31, 32). At normal incidence, the transmission resonances corresponding to $(0, \pm 1)$, $(+1, 0)$ and $(-1, 0)$ grating orders at the metal/air interface are nearly degenerate and polarization independent (Fig. 2B). The dispersion of the modes with the varying angles of incidence is due to the changing horizontal projection of the incident wavevector (\vec{k}_x). As shown in Fig. 2B, the $(0, \pm 1)$ modes have minimal dispersions for small angles of incidence, because \vec{k}_x and \vec{G}_y are perpendicular to each other. Dispersions of the $(\pm 1, 0)$ modes are quite large, because \vec{k}_x and \vec{G}_x are parallel. Fig. 2C shows the FDTD calculated spectral characteristics of the transmitted signals for varying angles of in-

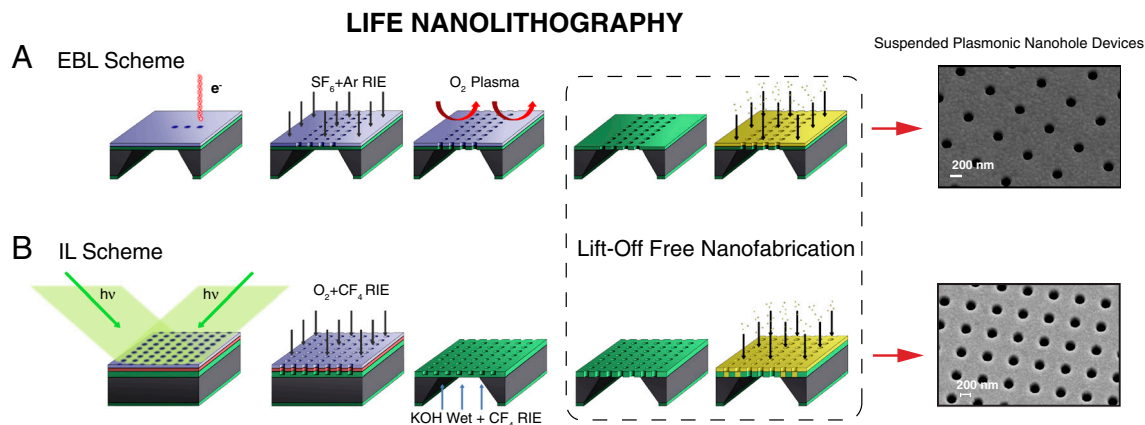


Fig. 1. Lift-off free evaporation (LIFE) nanolithography is summarized for schemes based on (A) electron-beam and (B) interference lithography. SEM images of the fabricated devices are shown for (A) $p = 600$ nm, $d = 180$ nm and (B) $p = 580$ nm and $d = 230$ nm, where p is the lattice periodicity and d is the nanohole diameter.

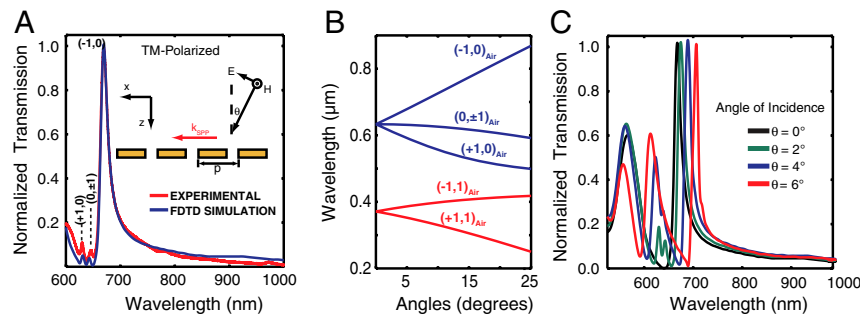


Fig. 2. (A) Experimentally (red curve) and numerically (blue curve) obtained EOT spectra are compared. The resonance peaks corresponding to the metal/air interface are indicated. (B) Spectral dispersion of the transmission minima is presented as a function of the angle of incidence for different grating orders. (C) EOT spectra is shown for varying angles of incidence using FDTD analysis.

cidence. For perpendicularly incident light ($\theta = 0^\circ$), $(0, \pm 1)$ and $(+1, 0)$ modes are subradiant as shown in Fig. 2C (black curve); i.e., they are weakly coupled to continuum. The $(-1, 0)$ mode, on the other hand, is superradiant; i.e., it is strongly coupled to continuum and radiative. When illuminated at a nonperpendicular incidence angle ($\theta \neq 0^\circ$), the retardation effects (field gradient created along the surface) allows coupling of the incident light to $(0, \pm 1)$ and $(+1, 0)$ dark modes (Fig. 2C). In our experimental measurements (Fig. 2A), splitting of these dark modes become observable at an angle of incidence $\theta \geq 1^\circ$ as confirmed by our FDTD simulations (Fig. 2A, dashed line). In agreement with the analytical predictions, $(+1, 0)$ modes show strong dependence to the angular incidence, whereas the $(0, \pm 1)$ modes are nearly independent and degenerate (Fig. 2C). For angles of incidence $\theta \geq 2^\circ$, continuum coupling to the $(+1, 0)$ mode becomes stronger leading to broader resonances and stronger spectral overlap with the $(0, \pm 1)$ modes. For angles of incidence $\theta \geq 6^\circ$, the $(0, \pm 1)$ modes becomes dark again. There exists a critical optical regime (angular incidence of $\theta \approx 1^\circ$) where the spectral overlap of the

$(+1, 0)$ and $(0, \pm 1)$ dark modes is small, whereas the incident light coupling to them is strong enough to allow modest light transmissions. By maintaining such alignment requirements, one can directly couple incident light to the spectrally narrow subradiant dark resonances. These experimentally observed features are explained in *SI Text* using leaky eigen-modes (Fig. S1 in *SI Text*).

Subradiant Plasmonic Resonances at the Drude Damping Limit. Subradiant nature of the $(0, \pm 1)$ and $(+1, 0)$ modes can be understood from the near-field characteristics of the surface plasmons at the air/metal interface (33, 34). H_y field profile of the SPP ($-1, 0$) mode for TM-polarized incident light (x -polarized) is shown in Fig. 3A. The standing field pattern (x-direction) in the background is due to the SPP excitations, whereas the enhanced hot spots around the rims of the nanoholes in the form a magnetic dipole are due to excitation of the localized surface plasmons (LSPs) (35). Near-field intensities of these local excitations dictate the coupling efficiency of the incident light to the Bloch

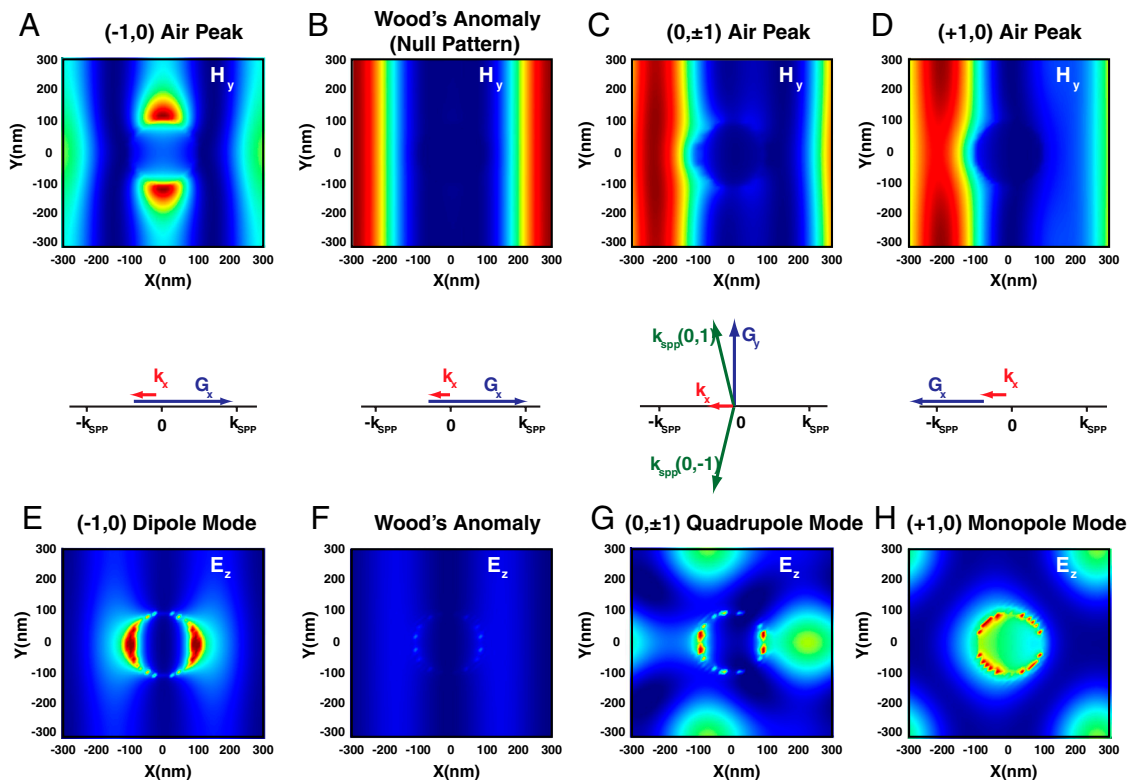


Fig. 3. Magnetic field profiles of (A) $(-1, 0)$ bright mode, (B) Wood's anomaly, (C) $(0, \pm 1)$ dark mode and (D) $(+1, 0)$ dark mode are shown. Electric field profiles reveal the (E) dipolar, (G) quadrupolar and (H) monopolar character of the $(-1, 0)$, $(0, \pm 1)$ and $(+1, 0)$ modes, respectively. (F) At Wood's anomaly excitation of the dipolar field mode is minimal however, finite.

mode of the nanohole openings, thus the strength of the resonant transmission (35). For the $(-1,0)$ mode, these local excitations have a dipolar mode character (Fig. 3E), which allows strong coupling of the incident light to the LSPs and leads to enhanced light transmissions in agreement with the experimental observations (Fig. 2). As shown in Fig. 3B, resonance transmission minimum responsible from the spectral Fano line-shape is due to the nearly null-field profile of the SPP excitation at the nanohole openings. This null pattern relates two fundamental observations: (i) weak coupling of the incident light to the Bloch mode of the nanohole openings leads to transmission minimum (Fig. 3F); (ii) SPP dispersion relations are minimally affected by the lower air-hole conductivities at the resonance minimum due to the negligible overlap of the SPP with the holes (36). Hence, the resonance minima are observed when the Bragg condition corresponding to the excitation of SPPs on a flat unperturbed surface is met (36). As shown in Fig. 2C (black curve), $(0, \pm 1)$ and $(+1,0)$ modes are subradiant for the perpendicularly incident light; i.e., radiative couplings are minimal. However, for incident light impinging with a small angle of incidence to the normal ($\theta \approx 1^\circ$), the introduced field gradient (retardation effects) enables coupling of the dipolar incident field to the dark modes that have no net-dipole moments (Fig. 3C and D). Field profiles of the $(0, \pm 1)$ and $(+1,0)$ dark modes confirming their quadrupole and monopole character are given in Fig. 3G and H, respectively. As a result, additional transmission peaks appear for nonperpendicularly incident light as confirmed by the experimental measurements (Fig. 2C). Unlike previous studies based on nanoparticles and metamaterials, the spectral overlap of the dipolar superradiant $(-1,0)$ mode to monopolar/multipolar subradiant $(+1,0)/(0, \pm 1)$ modes is minimal (Fig. 2A). In other words, in-direct coupling of the incident light to the subradiant modes through the superradiant mode is negligible (Fig. 3G and H). This leads high-quality factor ($Q_{(0,\pm 1)}^{\text{sub}} \approx 100$ and $Q_{(+1,0)}^{\text{sub}} \approx 200$) resonances. Close agreement with the experimental measurements and the numerical simulations is observed (Fig. 2A) without employing any enhanced damping constants for the thin gold films.

Ultrasensitive Plasmonic Nanosensors. Intrinsic detection limits of the resonance based biosensors are dictated by the spectral line-widths of the resonances and the refractive index sensitivities of the resonance wavelengths (17). In Fig. 4, refractive index sensitivities are obtained using NaCl solutions (Sigma-Aldrich 99.5%) at varying concentrations (5%, 10%, 15%, 20%) in deionized (DI) water with the corresponding refractive indices (1.3418, 1.3505, 1.3594, 1.3684) obtained at room temperature. As shown in Fig. 4A, *Inset*, the plasmonic resonances are fitted to an analytical Fano interference model (32) given as

$$T(\omega) = T_0 + A \left[\left(1 + \sum_{\nu} \frac{q_{\nu}}{\Delta \varepsilon_{\nu}} \right)^2 / \left(1 + \left(\sum_{\nu} \frac{q_{\nu}}{\Delta \varepsilon_{\nu}} \right)^2 \right) \right], \quad [1]$$

where $\Delta \varepsilon_{\nu} = 2\hbar(\omega - \omega_{\nu})/\Gamma_{\nu}$, T_0 is the transmission offset, A is the continuum-discrete coupling constant, ω_{ν} is the resonant frequency, Γ_{ν} is the full width at half maximum (FWHM) of the resonance and q_{ν} is the Breit-Wigner-Fano parameter determining asymmetry of the resonance profile for the ν th resonance state. Experimentally obtained sensor parameters are summarized in Table S1 (SI Text). Interferometric LIFE-lithography of plasmonic nanostructures is shown to yield wafer-scale fabrication of nanohole sensors with the similar optical qualities of the EBL fabricated ones (Fig. S2 in SI Text). Refractive index sensitivities as high as 717 nm are obtained (Fig. 4C). Remarkably narrow plasmonic resonances with 4.29 nm ($Q_{(+1,0)}^{\text{sub}} = 196.9$) are shown in solution (DI water with 10% NaCl). Overall performances of the biosensors are often quantified by a general figure of merit $\text{FOM}_E = S_{ij}(\text{eV RIU}^{-1})/\Gamma_{\nu}(\text{eV})$ in energy units, which is the refractive index sensitivity $S_{ij}(\text{eV RIU}^{-1})$ of the resonance frequency divided by the resonance width $\Gamma_{\nu}(\text{eV})$ of the plasmonic resonance (17). This quantity is widely accepted as a proper measure for the performance of plasmonic biosensors based on localized and extended surface plasmons (17, 21, 37, 38). In accordance with the observed spectrally narrow resonances, experimental FOM_E s as high as 144.28 are obtained for the subradiant $(+1,0)$ mode (see Table S1), a record high figure showing an order of magnitude improvement over the reported values for plasmonic sensor based on nanoparticles and metamaterials (21, 37, 39). Due to high optical quality of the fabricated devices enabled by LIFE lithography, even the superradiant $(-1,0)$ modes are shown to have record high experimental figures of merit ($\text{FOM}_E \approx 43$) (38).

Surpassing the Detection Limits of Gold Standard SPR Sensors. Prism coupled surface plasmon resonance (SPR) sensing is the gold standard technique for real-time, label-free measurement of biomolecular interactions, and plays an important role in drug discovery and biomedical research (25). Any alternative modality must be advantageous in its intrinsic detection limits. Nanohole based plasmonic sensors have recently taken much interest due to their ultrasmall interrogation volumes and (near) collinear illumination settings. Normal excitation of SPPs by grating-coupling in nanohole arrays holds the promise for massive multiplexing. However, plasmonic nanohole sensors have not been widely adapted as a result of broader resonance line-widths and lower spectral resolutions due to larger radiative losses. The widely adapted metric for the intrinsic resolving power of the prism coupled SPR sensors is the figure of merit $\text{FOM} = S_{ij}(\text{nm RIU}^{-1})/\Gamma_{\nu}(\text{nm})$ in wavelengths units, defined as the refractive index sensitivity $S_{ij}(\text{nm RIU}^{-1})$ of the resonance frequency divided by the spectral width $\Gamma_{\nu}(\text{nm})$ of the resonance. As listed in Table S1, the obtained figure of merit ($\text{FOM} = 162$ in wavelength units) for the $(+1,0)$ subradiant dark mode is higher than the theoretically estimated upper limits ($\text{FOM} = 108$) of the gold standard SPR sensors

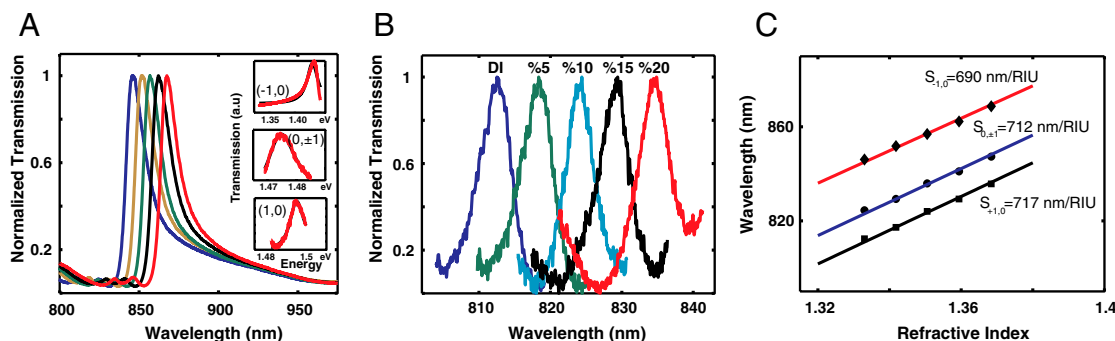


Fig. 4. (A) Spectral measurements are obtained with the varying concentrations of NaCl for devices fabricated with IL-based scheme. (B) Resonance shift is shown in detail for the subradiant $(+1,0)$ SPP mode with changing NaCl concentration. (C) Sensitivity of the devices are obtained using a linear fitting scheme.

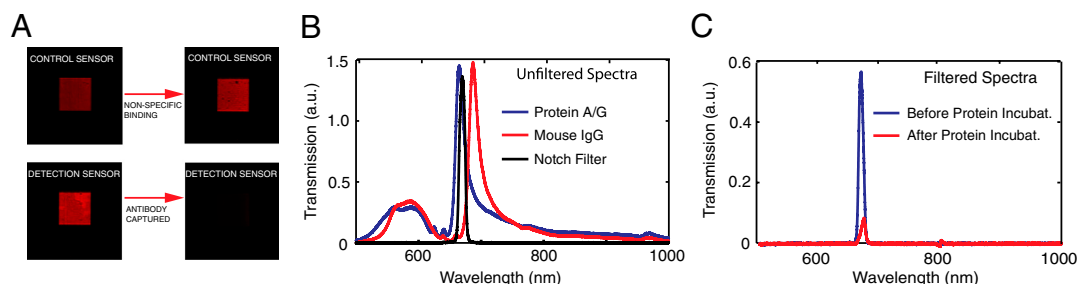


Fig. 5. Extremely sharp plasmonic Fano resonances in high-quality nanohole sensors enable seeing single biomolecular monolayers with naked eye. (A) CCD images of the transmitted light obtained from detection and control sensors are compared. Capturing of the antibody causes a dramatic reduction of the transmitted light intensities through the detection sensors. (B) Transmission spectra are shown before (blue curve) and after (red curve) the capturing of the antibody. Spectral characteristic of the notch filter is also given (green curve). (C) Transmitted light intensities in the presence of the notch filter is given before (blue curve) and after (red curve) the capturing of the antibody.

(25, 26) as well as nearly an order of magnitude larger than the previously reported record high FOMs in nanohole sensors using perpendicularly incident light (38).

Seeing Biomolecular Monolayers with Naked Eye. State-of-art detection platforms require mechanical or light isolation as well as expensive detection instrumentation for signal transduction. In our sensing platform, the superradiant modes ($-1,0$) have strong coupling to the dipolar incident light leading to extraordinary light transmission. This strong signal could be easily detected by eye and discernible in ordinary laboratory conditions without any mechanical/light isolation. An experimental demonstration of this with end-point measurements is summarized in Fig. 5. Initially the surfaces are activated and functionalized using a scheme summarized in an earlier study (27). Protein A/G (Pierce) is chosen as the capturing molecule due to its high affinity to IgG immunoglobulins. Blue curve in Fig. 5B shows the transmission spectra of a functionalized biosensor acquired from a nanohole array of $90\ \mu\text{m} \times 90\ \mu\text{m}$ in dimensions. A notch filter (FWHM $\approx 10\ \text{nm}$) spectrally tuned to the plasmonic resonances peak is used to filter the light outside resonant transmission peak of the bright ($-1,0$) mode (black curve in Fig. 4B). CCD images of the transmitted light are shown in Fig. 5A, in addition to images obtained from an unfunctionalized control sensor. As shown in Fig. 5B, capturing of a single monolayer of mouse IgG antibody (Sigma-Aldrich) causes 22 nm red shifting of the plasmonic resonance. This resonance shift is large enough to cause spectral overlapping of the transmission minima (Wood's anomaly) of the nanohole array with the transmission window of the notch filter (Fig. 5C). Accordingly, a dramatic reduction in transmitted light intensities is observed after the capturing of a monolayer of the antibody. This intensity change is strong enough to discern with naked eye in ordinary laboratory settings (Fig. 5A). For the control sensors (Fig. 5C), spectral shift is minimal due to nonspecific bindings causing negligible change in the transmitted light intensities (27). This detection scheme, not requiring dark-environment measurements, utilizes broad-band light sources allowing direct detection with human eye without any safety concerns. The transmitted light spectrum through the superradiant modes is dependent on the angle of incidence (Fig. 2C). As a result, the proposed detection scheme could be implemented by utilizing nearly collimated light obtained from an integrated light emitting diode for user

independent measurements. Sensing surfaces employing gold are inert to the environment. No degradation of device characteristics (Q -factors and FOMs) is observed over extended periods of time. Antibodies functionalized on the device surfaces are observed to be stable without any sign of significant denaturalization up to 10 days at ordinary storage conditions for biomolecules.

Conclusions

We introduced an ultrasensitive label-free biodetection technique based on Fano resonances in plasmonic nanohole devices. By utilizing spectrally sharp extraordinary light transmissions through subradiant dark modes, we showed record high experimental figures of merit (FOMs as high as 162) for detection limits surpassing that of the gold standard prism coupled surface plasmon sensors. To achieve this, we developed a high-throughput LIFE nanolithography technique leading to spectrally narrow subradiant dark resonances (FWHM of $\leq 4.26\ \text{nm}$) with nearly complete suppression of the radiative losses and high-quality factors ($Q_{(+1,0)}^{\text{sub}} \approx 200$). We also demonstrated direct detection of a monolayer of antibodies with naked eye by exploiting strongly dispersive plasmonic Fano resonances and the associated Wood's anomalies. The demonstrated label-free sensing platform offers unique opportunities for detection of biologically important molecules and pathogens in resource poor settings by eliminating the need for labeling and optical detection instruments as well as mechanical/light isolation.

Materials and Methods

LIFE Lithography. Nanohole devices were fabricated in a lift-off free manner on suspended SiN_x membranes by using a single layer deposition process as described in *SI Text*.

Spectral Measurements. All spectral data were obtained using a Nikon Eclipse-Ti microscope coupled to a SpectraPro 500i spectrometer and a Princeton Instruments Acton CCD camera.

ACKNOWLEDGMENTS. This work is supported in part by the National Science Foundation (NSF) CAREER Award (ECCS-0954790), the Office of Naval Research (ONR) Young Investigator Award, the Massachusetts Life Science Center New Investigator Award, the NSF Engineering Research Center on Smart Lighting (EEC-0812056), Boston University Photonics Center, and the Army Research Laboratory.

1. Lal S, Link S, Halas NJ (2007) Nano-optics from sensing to waveguiding. *Nat Photonics* 1:641–648.
2. Schuller JA, et al. (2010) Plasmonics for extreme light concentration and manipulation. *Nat Mater* 9:193–204.
3. Atwater HA, Polman A (2010) Plasmonics for improved photovoltaic devices. *Nat Mater* 9:205–213.
4. Luk'yanchuk B, et al. (2010) The Fano resonance in plasmonic nanostructures and metamaterials. *Nat Mater* 9:707–715.
5. Engheta N (2007) Circuits with light at nanoscales: Optical nanocircuits inspired by metamaterials. *Science* 317:1698–1702.
6. Genet C, Ebbesen TW (2007) Light in tiny holes. *Nature* 445:39–46.
7. Pendry JB (2000) Negative refraction makes a perfect lens. *Phys Rev Lett* 85:3966–3969.
8. Schurig D, et al. (2006) Metamaterial electromagnetic cloak at microwave frequencies. *Science* 314:977–980.
9. Kim S, et al. (2008) High-harmonic generation by resonant plasmon field enhancement. *Nature* 453:757–760.
10. MacDonald KF, Samson ZL, Stockman MI, Zheludev NI (2009) Ultrafast active plasmonics. *Nat Photonics* 3:55–58.
11. Kinkhabwala A, et al. (2009) Large single-molecule fluorescence enhancements produced by a bowtie nanoantenna. *Nat Photonics* 3:654–657.

12. Kneipp K, et al. (1997) Single molecule detection using surface-enhanced raman scattering (SERS). *Phys Rev Lett* 78:1667–1670.
13. Kundu J, Le F, Nordlander P, Halas NJ (2008) Surface enhanced infrared absorption (SEIRA) spectroscopy on nanoshell aggregate substrates. *Chem Phys Lett* 452:115–119.
14. Adato R, et al. (2009) Ultra-sensitive vibrational spectroscopy of protein monolayers with plasmonic nanoantenna arrays. *Proc Natl Acad Sci USA* 106:19227–19232.
15. Cubukcu E, Zhang S, Park Y-S, Bartal G, Zhang X (2009) Split ring resonator sensors for infrared detection of single molecular monolayers. *Appl Phys Lett* 95:043113–043113.
16. Neubrech F, et al. (2008) Resonant Plasmonic and Vibrational Coupling in a Tailored Nanoantenna for Infrared Detection. *Phys Rev Lett* 101:157403.
17. Sherry LJ, et al. (2005) Localized surface plasmon resonance spectroscopy of single silver nanocubes. *Nano Lett* 5:2034–2038.
18. Baptiste Augui, Barnes WL (2008) Collective resonances in gold nanoparticle arrays. *Phys Rev Lett* 101:143902.
19. Nagpal P, Lindquist NC, Oh S-H, Norris DJ (2009) Ultrasoft patterned metals for plasmonics and metamaterials. *Science* 325:594–597.
20. Fano U (1961) Effects of configuration interaction on intensities and phase shifts. *Physical Review* 124:1866–1878.
21. Liu N, et al. (2010) Planar metamaterial analogue of electromagnetically induced transparency for plasmonic sensing. *Nano Lett* 10:1103–1107.
22. Artar A, Yanik AA, Altug H (2011) Multispectral plasmon induced transparency in coupled meta-atoms. *Nano Lett* 11:1685–1689.
23. Zhang S, Genov DA, Wang Y, Liu M, Zhang X (2008) Plasmon-induced transparency in metamaterials. *Phys Rev Lett* 101:047401.
24. Hao F, et al. (2008) Symmetry breaking in plasmonic nanocavities: Subradiant LSPR sensing and a tunable Fano resonance. *Nano Lett* 8:3983–3988.
25. Phillips K (2008) Surface plasmon resonance-based sensors. *Anal Bioanal Chem*, ed Jiri Homola 390:1221–1222.
26. Tetz KA, Pang L, Fainman Y (2006) High-resolution surface plasmon resonance sensor based on linewidth-optimized nanohole array transmittance. *Opt Lett* 31:1528–1530.
27. Yanik AA, et al. (2010) An optofluidic nanoplasmonic biosensor for direct detection of live viruses from biological media. *Nano Lett* 10:4962–4969.
28. Gordon R, Brolo AG, Sinton D, Kavanagh KL (2010) Resonant optical transmission through hole-arrays in metal films: Physics and applications. *Laser Photon Rev* 4:311–335.
29. Yanik AA, Huang M, Artar A, Chang T-Y, Altug H (2010) Integrated nanoplasmonic-nanofluidic biosensors with targeted delivery of analytes. *Appl Phys Lett* 96:021101–021103.
30. Palik ED *Handbook of Optical Constants of Solids* (Elsevier, Amsterdam).
31. Ebbesen TW, Lezec HJ, Ghaemi HF, Thio T, Wolff PA (1998) Extraordinary optical transmission through sub-wavelength hole arrays. *Nature* 391:667–669.
32. Sarrazin M, Vigneron J-P, Vigoureux J-M (2003) Role of Wood anomalies in optical properties of thin metallic films with a bidimensional array of subwavelength holes. *Phys Rev B* 67:085415.
33. Yanik AA, Adato R, Erramilli S, Altug H (2009) Hybridized nanocavities as single-polarized plasmonic antennas. *Opt Express* 17:20900–20910.
34. Yanik AA, Wang X, Erramilli S, Hong MK, Altug H (2008) Extraordinary mid-infrared transmission of rectangular coaxial nanoaperture arrays. *Appl Phys Lett* 93:081104–081103.
35. Lalanne P, et al. (2005) Surface plasmons of metallic surfaces perforated by nanohole arrays. *J Opt A-Pure Appl Op* 7:422–426.
36. Liu H, Lalanne P (2008) Microscopic theory of the extraordinary optical transmission. *Nature* 452:728–731.
37. Mirin NA, Bao K, Nordlander P (2009) Fano resonances in plasmonic nanoparticle aggregates. *J Phys Chem A* 113:4028–4034.
38. Henzie J, Lee MH, Odom TW (2007) Multiscale patterning of plasmonic metamaterials. *Nat Nanotechnol* 2:549–554.
39. Liao H, Nehl CL, Hafner JH (2006) Biomedical applications of plasmon resonant metal nanoparticles. *Nanomedicine* 1:201–208.